Radiometric Cross-Calibration of GF-6/WFV Sensor Using MODIS Images With Different BRDF Models

Jie Han, Zui Tao, Yong Xie, Huina Li, Xiaoguo Guan, Hang Yi, Tingting Shi, and Gengke Wang

***Abstract*— The wide field of view (WFV) imaging system of the GaoFen-6 (GF-6) satellite processes four popular spectral bands [blue, green, red, and near-infrared (NIR)] and four new spectral bands (costal, yellow, and two red edges). However, the corresponding reference spectral bands for these eight spectral bands from one reference sensor are insufficient in the cross-calibration process of the WFV; therefore, current cross-calibration methods should be improved. To address this problem, the Moderate-Resolution Imaging Spectroradiometer (MODIS), which has high radiometric performance with the aid of an onboard calibration system, is used as a reference sensor, and cross-calibration methods using the top of atmosphere (TOA) and the bottom of atmosphere (BOA) bidirectional reflectance distribution function (BRDF) models are developed and compared. The results reveal that the cross-calibration results in eight spectral bands with the BOA BRDF model that can obtain higher consistency with the official calibration coefficients (OCCs) compared with the TOA BRDF model. In addition, after various influencing factors are comprehensively analyzed, the spectral band adjustment factor (SBAF) correction in the shortwave infrared (SWIR) spectral bands can be neglected; moreover, by using five spectral bands (blue, green, red, NIR, and SWIR) of the MODIS sensor, the BOA BRDF model and the cubic polynomial interpolation method provide optimal cross-calibration schemes for WFV sensor. The total radiometric cross-calibration uncertainties of the proposed cross-calibration methods with the BOA BRDF model and the TOA BRDF model are less than 5.73% and 6.32%, respectively.**

***Index Terms*— Bidirectional reflectance distribution function (BRDF) model, cross-calibration, GaoFen-6 (GF-6), Moderate-Resolution Imaging Spectroradiometer (MODIS), spectral interpolation.**

Manuscript received January 21, 2022; revised March 14, 2022; accepted April 14, 2022. Date of publication April 21, 2022; date of current version May 4, 2022. This work was supported in part by the National Key Research and Development Program of China-Joint Validation of Multi-Source Remote Sensing Information and Sharing in Brazil, Russia, India, China, and South Africa (BRICS) Countries under Grant 2018YFE0124200, in part by the National Natural Science Foundation Cultivation Project of Xuchang University under Grant 2022GJPY007, in part by the Science and Technology of Henan Province under Grant 212102310029 and Grant 222102320307, in part by the National Natural Science Foundation of China under Grant 42176176, in part by the Land Observation Satellite Supporting Platform of National Civil Space Infrastructure Project, in part by the Technical Pre-Research Project of Civil Aerospace under Grant D040401, and in part by the Key Scientific Research Project Plan of University in Henan Province under Grant 21B420003. *(Corresponding author: Yong Xie.)*

Jie Han, Xiaoguo Guan, and Hang Yi are with the School of Urban and Environment Sciences, Xuchang University, Xuchang 461000, China (e-mail: hanjie@radi.ac.cn; guanguo666@163.com; yihang@xcu.edu.cn).

Zui Tao and Gengke Wang are with the Aerospace Information Research Institute, Chinese Academy of Sciences, Beijing 100101, China (e-mail: taozui@radi.ac.cn; wanggk@aircas.ac.cn).

Yong Xie is with the School of Geography and Remote Sensing, Nanjing University of Information Science and Technology, Nanjing 210044, China (e-mail: xieyong@nuist.edu.cn).

Huina Li is with the School of Electrical and Mechanical Engineering (Engineering Training Center), Xuchang University, Xuchang 461000, China (e-mail: lihuina851013@163.com).

Tingting Shi is with the State Key Laboratory of Dao-di Herbs, National Resource Center for Chinese Materia Medica, China Academy of Chinese Medical Sciences, Beijing 100700, China (e-mail: shi_tingt@163.com).

Digital Object Identifier 10.1109/TGRS.2022.3169211

I. Introduction

DUE to changes in the operation environment, such as drastic temperature changes and intense electromagnetic radiation, the radiometric performance of sensor after successfully launched into space will be changed [1]. Therefore, on-orbit radiometric calibration coefficients of satellite sensors should be regularly updated and released to ensure the quantitative application level of satellite imagery during the orbital lifetime and the establishment of links between the satellite signal and the quantitative remote sensing parameters [2], [3].

Although many radiometric calibration methods have been developed, the cross-calibration method is a good strategy to implement for orbital radiometric calibration of satellite sensors without onboard calibration assembly because this method requires less human and material resources, yields higher calibration frequencies, and ensures convenient recalibration for historical satellite images [4]. For instance, taking Moderate-Resolution Imaging Spectroradiometer (MODIS) as the radiometric reference, Liu *et al.* [5] implemented the long-term cross-calibration of the huanjing-1A (HJ-1A)/charge-coupled device (CCD1) sensor and discussed the radiometric attenuation of this sensor after 12 years of on-orbit operation. Since GF-4/panchromatic and multispectral sensors (PMSs) utilize five different integration times, Han *et al.* [6] developed a cross-calibration method based on radiometric block adjustment to simultaneously achieve high absolute radiometric calibration consistency with official calibration coefficients (OCCs) and reduce the radiometric difference between PMS images at different integration times. Taking an instrumented sand site as the radiometric-transfer platform, Zhao *et al.* [7] fulfilled the cross-calibration of the GF-1/PMS and used the OCCs to validate the cross-calibration accuracy. Angal *et al.* [8] evaluated the radiometric calibration agreement between MODIS and Enhanced Thematic Mapper Plus (ETM+) over Libya 4 site with the cross-calibration method. Zhou *et al.* [9] developed an improved cross-calibration method with the mean value spectral matching approach to obtain high-accuracy calibration coefficients for GF-4/infrared spectrum (IRS) sensor. Considering the characteristics of large view angles, Zhou *et al.* [10] adopted global searching

algorithms to calibrate GF-1/wide field of view (WFV1) and GF-4/PMS with Landsat-8/operational land imager (OLI). Niu *et al.* [11] applied the cross-calibration method to calibrate the ziyuan1-02D (ZY1-02D) hyperspectral imager using the well-calibrated GF-5/advanced hyperspectral imager (AHSI) sensor. Zhou *et al.* [12] comprehensively discussed the influence of the bidirectional reflectance distribution function (BRDF) over deserts and forests on the cross-calibration results. To evaluate the annual change of Huanjing-1B (HJ-1B)/IRS during its orbital lifetime, Liu *et al.* [13] carried out cross-calibration of IRS with MODIS images over the Lake Qinghai site. In the cross-calibration process of the Landsat-8/OLI and Sentinel-2A/multispectral instrument (MSI) sensors, Farhad *et al.* [14] proposed a new four-angle site-specific BRDF model to fulfill the BRDF correction.

Previous studies on radiometric cross-calibration show that the reference sensor and the calibrated sensor should utilize similar spectral band settings. Unfortunately, the corresponding reference spectral bands of the eight-band GaoFen-6 (GF-6)/WFV sensor are simultaneously unavailable from one reference sensor. Consequently, only the radiometric performance attenuation of the GF-6/WFV sensor in four popular spectral bands is evaluated with MODIS, Landsat 8/OLI, and Sentinel-2/MSI sensors [15]. Although Han *et al.* [16] attempted to address this problem with the spectral interpolation method, only the radiometric cross-calibration method with the bottom of atmosphere (BOA) BRDF model was preliminarily applied on five calibrated days. Therefore, the radiometric cross-calibration methods with the BOA and top of atmosphere (TOA) BRDF models are comprehensively compared on a greater number of calibrated days to analyze the applicability and stability of two radiometric cross-calibration methods for the GF-6/WFV sensor. The research results will help identify an optimal cross-calibration scheme for GF-6/WFV sensor to further fulfill the radiometric degradation detection of this sensor during its orbital lifetime.

The organization of this article is as follows. Section II provides information of the calibrated WFV sensor, the well-calibrated MODIS sensor, the Dunhuang radiometric calibration site (DRCS), and the valid image pairs. Section III presents the construction process of the TOA and BOA BRDF models, the spectral matching approach, and the radiometric cross-calibration principle with the BOA and TOA BRDF models. Section IV illustrates the consistency between the radiometric cross-calibration results obtained with different BRDF models and the OCCs. Section V focuses on the various influencing factors in our cross-calibration process and calculates the total calibration uncertainties of the radiometric cross-calibration methods with the TOA and BOA BRDF models. Section VI summarizes our research, presents related conclusions, and provides recommendations for future studies.

II. Satellites, Test Site, and Datasets

A. Satellites

The GF-6 satellite, launched on June 2, 2018, is designed for precision agriculture and vegetation research, which is designed for an eight-year life time [15], [17], [18]. The WFV sensor on board the GF-6 satellite can acquire multispectral imagery with eight spectral bands (blue, green, red, near-infrared (NIR), costal, yellow, and two red-edges), 16-m ground sample distance (GSD), 800-km swath, and 12-bit quantization. The equator crossing time of GF-6 satellite is 10:30 local standard time. Recently, the GF-1 and GF-6 satellites have developed networking satellite constellations to acquire earth observation remote sensing imagery with a two-day revisit period. Since the size of one GF-6/WFV image is more than 13 GB, these images are segmented into three subimages for convenient data transmission and processing. The China Centre for Resources Satellite Data and Application (CRESDA) is responsible for GF-6 data distribution and preprocessing.

TABLE I
Main Sensor Parameters of WFV and MODIS

Sensor	Spectral Band Number	Spectral Range (nm)	Quantization (bits)	GSD (m)	Swath (km)	Altitude (km)
WFV	1	450-520	12	16	800	644.5
	2	520-590				
	3	630-690				
	4	770-890				
	5	690-730				
	6	730-770				
	7	400-450				
	8	590-630				
MODIS	1	620-670	12	500	2330	705
	2	841-876				
	3	459-479				
	4	545-565				
	5	1230-1250				

The MODIS sensor is a key instrument aboard the Terra satellite launched on December 18, 1999. The primary mission of MODIS is to acquire remote sensing data in 36 spectral bands, which are mainly used to predict global change and monitor atmospheric pollution. With the help of the onboard calibration system, the MODIS sensor can acquire high-accuracy radiometric data, which makes the MODIS sensor a well-calibrated sensor to provide radiometric reference information in the cross-calibration process [5], [6], [19]. Meanwhile, the Level-1 and atmosphere archive and distribution system can distribute the MODIS science data and related land surface and atmospheric parameter products.

In this study, five spectral bands of the MODIS sensor are selected to implement the radiometric cross-calibration of the GF-6/WFV. Table I lists the spectral range, orbit altitude, GSD, swath, and quantization level of the WFV and MODIS sensors. Fig. 1 illustrates the relative spectral responses (RSRs) of the MODIS sensor in five spectral bands and the WFV in eight spectral bands.

B. Test Site

The DRCS is an important radiometric calibration site in China for the radiometric calibration of satellite sensors without the onboard calibration assembly [20]. The DRCS is located in the Gobi Desert of Dunhuang, Gansu, China. Fig. 2 shows that there is no vegetation, the terrain is flat, and the coverage of homogeneous surfaces is very large. Therefore, CRESDA implements annual site calibration and scholars have developed cross-calibration at this site to obtain

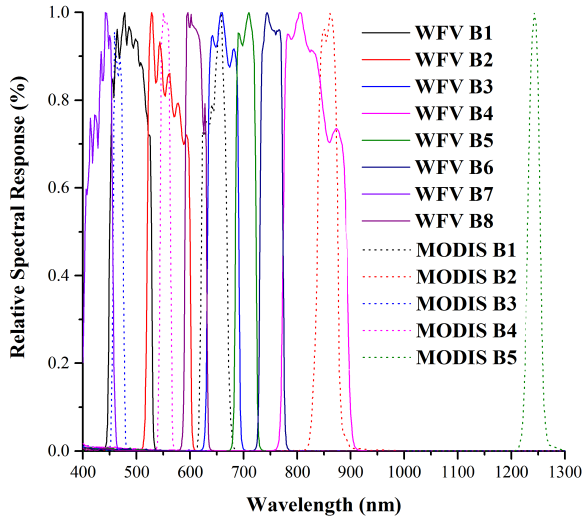

Fig. 1. RSRs of WFV and MODIS.

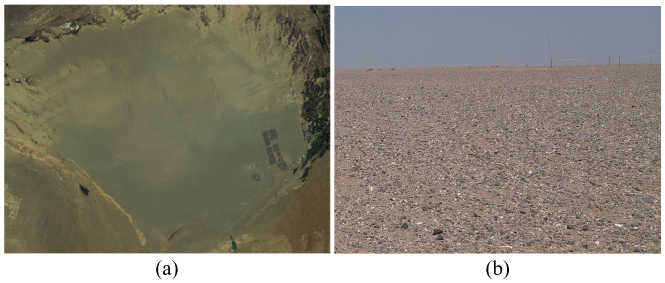

Fig. 2. Dunhuang test site: (a) GF-6/WFV image and (b) detailed landscape.

the on-orbit radiometric calibration coefficients and detect radiometric changes in the target sensor [5], [21].

C. Datasets

Valid cross-calibration image pairs are vital to the cross-calibration of the WFV sensor, which may affect the accuracy of the cross-calibration results and the reliability and stability of the cross-calibration method. In this study, valid image pairs over the DRCS on 19 days are collected based on the data filter criteria [22]. Fig. 3 illustrates the viewing geometries of the valid MODIS and WFV image pairs over the DRCS. The time intervals of the image pairs are all less than 1 h, as shown in Fig. 4. Since the aerosol optical thickness (AOT) at 550 nm is an important factor in the cross-calibration process, the corresponding AOT at 550-nm values is extracted from the MOD04_L2 products on the calibrated days shown in Fig. 5.

Cross-calibration information for MODIS and WFV images should be extracted based on the longitude and latitude of the investigated target. Since the geometric positioning accuracies of the WFV and MODIS are different, the subsequent geometric registration errors will affect the cross-calibration accuracy. Therefore, in our study, the averaged TOA and BOA spectral reflectance of 5 pixels × 5 pixels for the MOD02HKM and MOD09 data and the averaged digital number (DN) value of 156 pixels × 156 pixels for the WFV image over the center of the DRCS (approximately 2500 m × 2500 m) are extracted to implement the cross-calibration process.

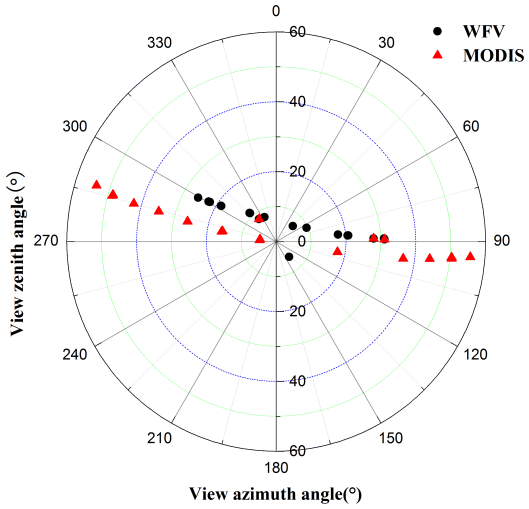

Fig. 3. Viewing geometries of MODIS and WFV.

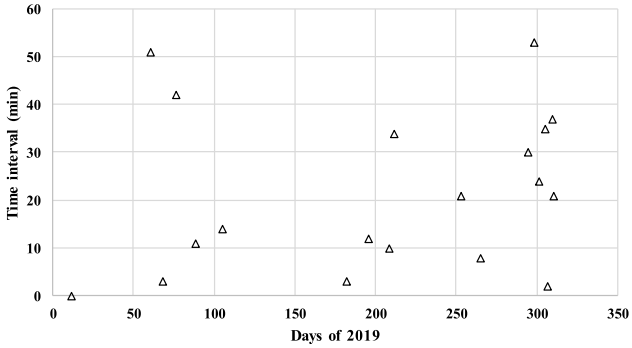

Fig. 4. Time interval between the two satellites overpassing DRCS on the calibrated days.

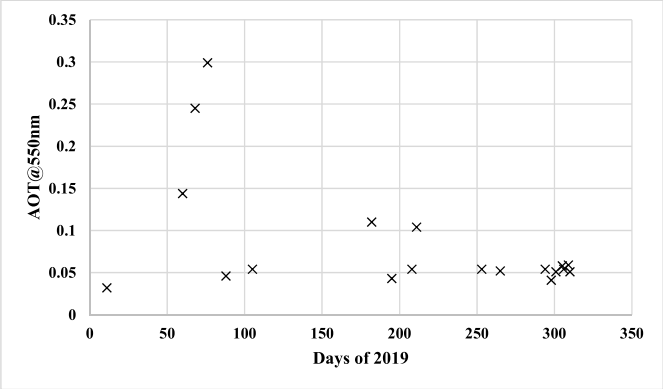

Fig. 5. AOT at 550 nm over the DRCS on the calibrated days.

Since the swath of MODIS is approximately 2330 km and that of the WFV is approximately 800 km, as listed in Table I, and the image coordinate of the investigated target is not fixed and changes on different calibrated days, the solar illumination and view geometries over the investigated target are notably different from those of the image center region. Therefore, to reduce the influence of solar and viewing geometry information errors on the cross-calibration results,

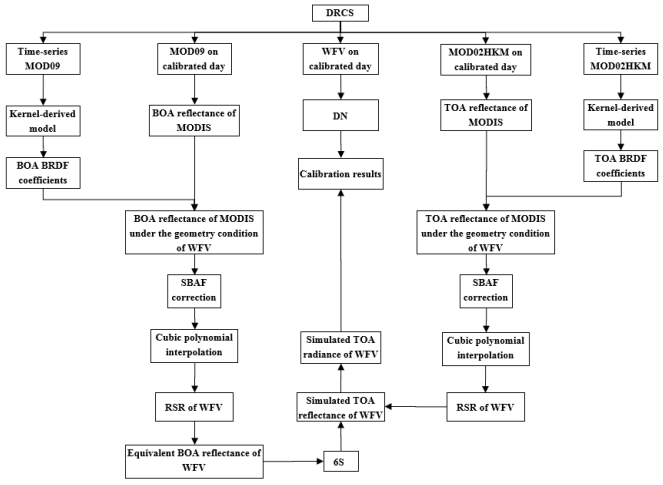

Fig. 6. Flowchart of the experiment.

the MOD03 product and the angle file of the WFV are used to provide accurate solar and viewing geometry information according to the geographical position of the investigated target [16].

III. Methodology

In this study, two radiometric cross-calibration methods with the BOA and TOA BRDF models are developed and compared to perform radiometric cross-calibration of the GF-6/WFV, even when partial reference spectral bands are lacking.

The main steps of the two radiometric cross-calibration methods with the BOA and TOA BRDF models, as illustrated in Fig. 6, are as follows.

1) The averaged BOA spectral reflectance and the TOA spectral reflectance of MODIS over the investigated target on the calibrated days are extracted from the corresponding MOD09 and MOD02HKM data.
2) The valid time-series MOD09 and MOD02HKM data over the DRCS in 2019 are used to obtain the BOA BRDF kernel-derived model coefficients and the TOA BRDF kernel-derived model coefficients with the Ross–Li BRDF model, respectively.
3) The BOA spectral reflectance and the TOA spectral reflectance of MODIS under the geometric condition of the WFV are derived with the BOA and TOA BRDF correction coefficients, respectively.
4) The spectral band adjustment factor (SBAF) correction is applied to compensate for the intrinsic offsets between the MODIS and WFV sensors caused by RSR mismatches.
5) The cubic polynomial interpolation method is used to obtain the interpolated continuous BOA and TOA spectral profile of the investigated target.
6) For the cross-calibration method with the TOA BRDF model, based on the interpolated continuous TOA spectral profile, the simulated TOA reflectance of the WFV in eight spectral bands is derived with the RSRs of the WFV. For the cross-calibration method with the BOA BRDF model, the equivalent BOA reflectance of the WFV in eight spectral bands should be converted to the simulated TOA reflectance with the aid of 6S radiative transfer model.
7) After the simulated TOA radiance is calculated, the cross-calibration coefficients are derived with the averaged DN value of the WFV over the investigated target on the calibrated days.

A. Construction Methods of the TOA and BOA BRDF Models

BRDF is a function of the sensor zenith angle θ_v, the solar zenith angle θ_s, and the relative azimuth angle ϕ, which can establish the quantitative relationship between the spectral reflectance and the illumination and viewing geometry [12]. Fig. 3 shows that the viewing geometries of the MODIS and WFV sensors over the investigated target are notably different. Therefore, the BRDF correction should be taken into account to reduce the influence of the viewing geometric difference on the cross-calibration results. However, the BRDF kernel-derived model coefficients in spectral bands 1–7 of MODIS provided by the MCD43A1 products are not available on the calibrated days over the DRCS. Therefore, in this study, two BRDF models based on the TOA spectral reflectance and the BOA spectral reflectance, the BOA BRDF model and the TOA BRDF model, are established using the Ross–Li BRDF model, as shown in the following equation, with MOD09 and MOD02HKM data [23]:

$$\rho(\theta_v, \theta_s, \phi) = f_{iso}(\lambda) + f_{geo}(\lambda)k_{geo}(\theta_v, \theta_s, \phi) + f_{vol}(\lambda)k_{vol}(\theta_v, \theta_s, \phi) \quad (1)$$

where $\rho(\theta_v, \theta_s, \phi)$ is the bidirectional spectral reflectance; f_{iso}, f_{geo}, and f_{vol} are the kernel-derived model coefficients; and k_{geo} and k_{vol} are calculated with the sensor zenith angle θ_v, the solar zenith angle θ_s, and the relative azimuth angle ϕ.

MODIS data over the DRCS in 2019 are filtered to obtain valid clear sky data that are not contaminated by cloud clusters and snow. Valid clear sky data from MOD09 and MOD02HKM on 104 days are collected. Then, the averaged BOA and TOA spectral reflectance over the investigated target are extracted from MOD09 and MOD02HKM, respectively. The corresponding observation geometry parameters are extracted from the MOD03 product. Finally, the averaged BOA and TOA spectral reflectance, solar and viewing geometry parameters are input into (1) to obtain the BOA and TOA BRDF kernel-derived model coefficients f_{iso}, f_{geo}, and f_{vol} in the blue, green, red, NIR, and shortwave infrared (SWIR) spectral bands listed in Table II. Therefore, if the related angles (θ_v, θ_s, and ϕ) are given, the corresponding BOA or TOA spectral reflectance can be derived by (1) using the coefficients listed in Table II.

B. Spectral Matching

Although the spectral band ranges of the WFV and MODIS in the four popular spectral bands are similar, Fig. 1 illustrates that the RSRs of the WFV and MODIS sensors are different. Therefore, to reduce the influence of the RSR differences on the cross-calibration results, spectral matching using SBAF in these four spectral bands should be implemented [24].

TABLE II
BOA AND TOA BRDF KERNEL-DERIVED MODEL COEFFICIENTS OF DRCS

BRDF Model	BRDF Kernel-derived Model Coefficients	Blue	Green	Red	NIR	SWIR
BOA BRDF	f_{iso}	0.1779	0.2309	0.2673	0.2785	0.3056
	f_{vol}	0.0668	0.0951	0.1192	0.1359	0.1373
	f_{geo}	0.0166	0.0209	0.0247	0.0236	0.0283
TOA BRDF	f_{iso}	0.2092	0.2319	0.2565	0.2785	0.3106
	f_{vol}	0.2463	0.1509	0.1288	0.1397	0.1314
	f_{geo}	-0.0030	0.0175	0.0248	0.0253	0.0356

Due to the lack of the SWIR spectral band of the WFV, the SBAF correction in the SWIR spectral band is neglected and the corresponding SBAF correction coefficients in the SWIR spectral band are set to 1.0 in this study.

For the cross-calibration method with the TOA BRDF model, the simulated TOA reflectance of MODIS $\rho^{\text{M\_6S}}$ and WFV $\rho^{\text{W\_6S}}$ under the geometric condition of the WFV are derived with the aid of the 6S model, the viewing geometry of the WFV, and the historical measured averaged surface profile ρ^{ASD} using analytical spectral devices (ASDs) over the DRCS. It should be noted that the atmospheric condition is set to the midlatitude summer from April to September and midlatitude winter from October to March [5]. Meanwhile, the AOT at 550-nm values on calibrated days shown in Fig. 5 is extracted from the MOD04_L2 aerosol product. The aerosol type is set to desert, and the altitude of the DRCS is set to 1200 m. Then, the TOA SBAF correction coefficients $C_{\text{SBAF}}^{\text{TOA}}$ are calculated by the following equation:

$$C_{\text{SBAF}}^{\text{TOA}} = \frac{\rho^{\text{W\_6S}}}{\rho^{\text{M\_6S}}}. \tag{2}$$

For the cross-calibration method with the BOA BRDF model, the BOA SBAF correction coefficients $C_{\text{SBAF}}^{\text{BOA}}$ are derived by the following equation with the RSR of the WFV $\text{RSR}_{\text{WFV}}(\lambda)$, the RSR of MODIS$\text{RSR}_{\text{MODIS}}(\lambda)$, and the historical measured averaged surface profile ρ^{ASD} over the DRCS:

$$C_{\text{SBAF}}^{\text{BOA}} = \frac{\frac{\int \rho^{\text{ASD}} \times \text{RSR}_{\text{WFV}}(\lambda) d\lambda}{\int \text{RSR}_{\text{WFV}}(\lambda) d\lambda}}{\frac{\int \rho^{\text{ASD}} \times \text{RSR}_{\text{MODIS}}(\lambda) d\lambda}{\int \text{RSR}_{\text{MODIS}}(\lambda) d\lambda}}. \tag{3}$$

C. Cross-Calibration Model

According to the above-established BOA and TOA BRDF models and the spectral matching method, our cross-calibration models with the BOA and TOA BRDF models are developed in this section, which consists of the following six steps.

1) Use the BOA BRDF kernel-derived model coefficients listed in Table II to simulate the BOA spectral reflectance under the geometry condition of MODIS, $\rho_{\text{M\_brdf}}^{\text{BOA}}$, and that of the WFV under the geometry condition of the WFV, $\rho_{\text{W\_brdf}}^{\text{BOA}}$, with aid of the observation geometry parameters of the MODIS and WFV sensors. Then, the BOA BRDF correction coefficients $C_{\text{BRDF}}^{\text{BOA}}$ are derived by (4). Similar to $C_{\text{BRDF}}^{\text{BOA}}$, the TOA BRDF correction coefficients $C_{\text{BRDF}}^{\text{TOA}}$ are derived by (5) with the simulated TOA spectral reflectance under the geometric condition of MODIS, $\rho_{\text{M\_brdf}}^{\text{TOA}}$, and that of the WFV under the geometric condition of the WFV, $\rho_{\text{W\_brdf}}^{\text{TOA}}$

$$C_{\text{BRDF}}^{\text{BOA}} = \frac{\rho_{\text{W\_brdf}}^{\text{BOA}}}{\rho_{\text{M\_brdf}}^{\text{BOA}}} \tag{4}$$

$$C_{\text{BRDF}}^{\text{TOA}} = \frac{\rho_{\text{W\_brdf}}^{\text{TOA}}}{\rho_{\text{M\_brdf}}^{\text{TOA}}}. \tag{5}$$

2) Convert the averaged BOA spectral reflectance of MOD09 $\rho_{\text{MOD09}}^{\text{BOA}}$ over the investigated target in five spectral bands to the BOA spectral reflectance under the geometry condition of the WFV $\rho_{\text{W\_ref}}^{\text{BOA}}$ using the BOA BRDF correction coefficient $C_{\text{BRDF}}^{\text{BOA}}$ and the BOA SBAF correction coefficient $C_{\text{SBAF}}^{\text{BOA}}$ by the following equation:

$$\rho_{\text{W\_ref}}^{\text{BOA}} = C_{\text{BRDF}}^{\text{BOA}} \times C_{\text{SBAF}}^{\text{BOA}} \times \rho_{\text{MOD09}}^{\text{BOA}}. \tag{6}$$

The TOA spectral reflectance under the geometric condition of the WFV$\rho_{\text{W_ref}}^{\text{TOA}}$ is derived by the following equation with the averaged TOA spectral reflectance under the geometric condition of MODIS$\rho_{\text{MOD02HKM}}^{\text{TOA}}$, the TOA BRDF correction coefficient $C_{\text{BRDF}}^{\text{TOA}}$, and the TOA SBAF correction coefficient $C_{\text{SBAF}}^{\text{TOA}}$:

$$\rho_{\text{W\_ref}}^{\text{TOA}} = C_{\text{BRDF}}^{\text{TOA}} \times C_{\text{SBAF}}^{\text{TOA}} \times \rho_{\text{MOD02HKM}}^{\text{TOA}}. \tag{7}$$

3) To obtain the interpolated continuous BOA spectral profile $\rho_{\text{W\_Cref}}^{\text{BOA}}$ and the interpolated continuous TOA spectral profile $\rho_{\text{W\_Cref}}^{\text{TOA}}$ under the geometry conditions of the WFV, the cubic polynomial interpolation method is selected to fulfill the spectral interpolation, which is convenient to convert to the eight spectral bands information of the WFV from five spectral bands of MODIS.
4) For the cross-calibration method with the BOA BRDF model, the equivalent BOA spectral reflectance of the WFV $\rho_{\text{W\_Eref}}^{\text{BOA}}$ in eight spectral bands is first derived by the following equation. Then, the $\rho_{\text{W\_Eref}}^{\text{BOA}}$ value is converted to the simulated TOA spectral reflectance of the WFV $\rho_{\text{W\_Sref}}^{\text{TOA}}$ with the 6S model

$$\rho_{\text{W\_Eref}}^{\text{BOA}} = \frac{\int \rho_{\text{W\_Cref}}^{\text{BOA}} \times \text{RSR}_{\text{WFV}}(\lambda) d\lambda}{\int \text{RSR}_{\text{WFV}}(\lambda) d\lambda}. \tag{8}$$

For the cross-calibration method with the TOA BRDF model, the simulated TOA spectral reflectance of the WFV $\rho_{\text{W\_Sref}}^{\text{TOA}}$ is calculated by the following equation:

$$\rho_{\text{W\_Sref}}^{\text{TOA}} = \frac{\int \rho_{\text{W\_Cref}}^{\text{TOA}} \times \text{RSR}_{\text{WFV}}(\lambda) d\lambda}{\int \text{RSR}_{\text{WFV}}(\lambda) d\lambda}. \tag{9}$$

5) The final simulated TOA radiance of the WFV $L_{\text{WFV}}^{\text{TOA}}$ is derived by the following equation:

$$L_{\text{WFV}}^{\text{TOA}} = \frac{\rho_{\text{W\_Sref}}^{\text{TOA}} \times \text{ESUN}^{\text{W}} \times \cos\theta_{\text{s}}^{\text{W}}}{\pi d^2} \tag{10}$$

where ESUN^{W} is the exoatmospheric solar spectral irradiance of the WFV listed in Table III; d is the earth–sun distance, and $\theta_{\text{s}}^{\text{W}}$ is the solar zenith angle of the WFV image.
6) Since 2017, CRESDA has taken measures to eliminate the calibration coefficient offset of all GF series satellite

TABLE III
EXOATMOSPHERIC SOLAR SPECTRAL IRRADIANCE OF WFV

Spectral Band of WFV	1	2	3	4	5	6	7	8
$ESUN^W$ ($W \cdot m^{-2} \cdot \mu m^{-1}$)	1949.83	1845.44	1552.23	1073.01	1410.63	1267.46	1788.63	1735.38

TABLE IV
SDS OF THE CROSS-CALIBRATION COEFFICIENTS WITH DIFFERENT BRDF MODELS

Spectral Band of WFV	SDs	
	Cross-calibration coefficients with the BOA BRDF model	Cross-calibration coefficients with the TOA BRDF model
1	0.0018	0.0021
2	0.0014	0.0014
3	0.0010	0.0007
4	0.0006	0.0005
5	0.0021	0.0014
6	0.0012	0.0011
7	0.0040	0.0050
8	0.0012	0.0010

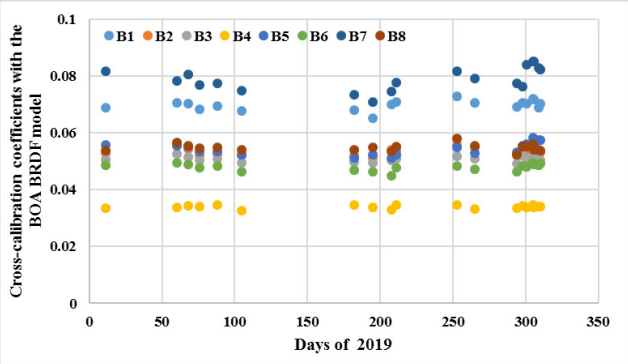

Fig. 7. Cross-calibration coefficients with the BOA BRDF model.

sensors in the data preprocessing process [15], [16]. The calibration coefficient offset is set to 0. Therefore, the cross-calibration coefficient gain of the WFV, Gain, is calculated by the following equation:

$$\text{Gain} = \frac{L_{\text{WFV}}^{\text{TOA}}}{\text{DN}^{\text{W}}} \tag{11}$$

where DN^W is the averaged DN value extracted from the WFV image over the investigated target on the calibrated day.

IV. RESULTS

A. Cross-Calibration Results With the BOA and TOA BRDF Models

Based on the above established radiometric cross-calibration methods with the BOA and TOA BRDF models, the calibration coefficients of the WFV with the BOA BRDF model and the TOA BRDF model are calculated and illustrated in Figs. 7 and 8, respectively. The corresponding standard deviations (SDs) of the cross-calibration coefficients are listed

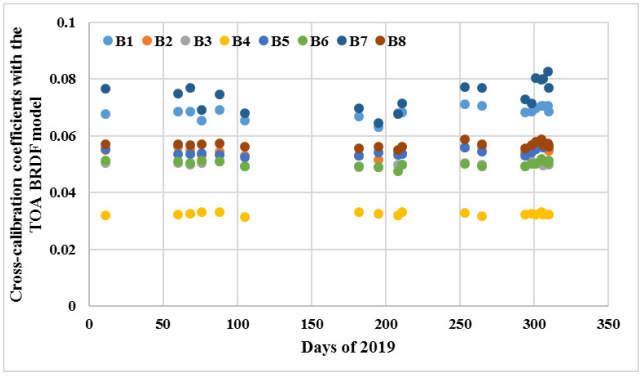

Fig. 8. Cross-calibration coefficients with the TOA BRDF model.

TABLE V
AVERAGED RELATIVE ERROR BETWEEN THE OCCS AND THE CROSS-CALIBRATION COEFFICIENTS WITH DIFFERENT BRDF MODELS

Spectral Band of WFV	OCCs	The Averaged Relative Error	
		Cross-calibration coefficients with the BOA BRDF model (%)	Cross-calibration coefficients with the TOA BRDF model (%)
1	0.0705	1.94	3.25
2	0.0567	5.67	3.37
3	0.0516	2.20	3.11
4	0.0322	5.37	1.34
5	0.0532	3.70	2.54
6	0.0453	5.61	10.77
7	0.0786	4.20	6.65
8	0.0585	6.48	3.05

in Table IV. The maximum SDs of the cross-calibration coefficients of the WFV with the BOA BRDF model and with the TOA BRDF model are 0.40% and 0.50% in spectral band 7 of the WFV, respectively, which indicates that the cross-calibration results with different BRDF models have good consistency, although the cross-calibration results with the BOA BRDF model are slightly more stable than those with the TOA BRDF model.

B. Validation Cross-Calibration Results With the OCCs

Although the cross-calibration results of the WFV with the BOA BRDF model are slightly more stable than those with the TOA BRDF model, the accuracy of the cross-calibration results with the BOA and TOA BRDF models must also be validated to further evaluate the reliability of the two cross-calibration methods.

Many previous studies on the cross-calibration validation of GF series satellite sensors have shown that the OCCs annually released by CRESDA with the site calibration method over DRCS have a sufficiently high accuracy [5], [7]. Therefore, the OCCs in this section are also treated as the reference to validate the cross-calibration results with the BOA and TOA BRDF models. The relative error is defined as the absolute value of "the cross-calibration coefficients/the OCCs -1." Then, the averaged relative errors between the OCCs and the cross-calibration coefficients are calculated, and they are listed in Table V.

TABLE VI

AVERAGED RELATIVE ERROR BETWEEN THE OCCS AND THE CROSS-CALIBRATION COEFFICIENTS WITH DIFFERENT BRDF MODELS ONLY USING FOUR POPULAR SPECTRAL BANDS OF MODIS

Spectral Band of WFV	The Averaged Relative Error	
	Cross-calibration Coefficients with the BOA BRDF Model (%)	Cross-calibration Coefficients with the TOA BRDF Model (%)
1	2.02	3.66
2	6.13	4.86
3	1.69	1.38
4	5.85	2.35
5	3.97	6.07
6	7.09	15.79
7	4.15	5.76
8	6.50	3.13

TABLE VII

AVERAGED RELATIVE ERROR BETWEEN THE OCCS AND THE CROSS-CALIBRATION COEFFICIENTS WITH DIFFERENT BRDF MODELS WITHOUT BRDF CORRECTION

Spectral Band of WFV	The Averaged Relative Error	
	Cross-calibration Coefficients with the BOA BRDF Model (%)	Cross-calibration Coefficients with the TOA BRDF Model (%)
1	5.31	10.80
2	7.36	9.11
3	7.10	7.97
4	10.15	8.64
5	9.57	9.60
6	10.70	14.79
7	5.76	13.68
8	8.10	8.32

Table V shows that the cross-calibration results of the WFV with the BOA BRDF model are closer to the OCCs than those with the TOA BRDF model. The maximum averaged relative errors of the cross-calibration results are 6.48% in spectral band 8 of the WFV and 10.77% in spectral band 6 of the WFV for the cross-calibration method with the BOA and TOA BRDF models, respectively. This finding indicates that the cross-calibration method with the BOA BRDF model is more suitable for WFV sensor, even when the corresponding available reference spectral bands are lacking.

V. DISCUSSION

A. WFV Calibrated With Only Four Spectral Bands of MODIS

In the proposed cross-calibration method, five spectral bands of MODIS (blue, green, red, NIR, and SWIR) are used to obtain the continuous BOA and TOA spectral profiles with the cubic polynomial interpolation method. In this section, whether reliable cross-calibration results can be obtained, using only the four popular spectral bands of MODIS (blue, green, red, and NIR) is discussed.

Compared with Table V, Table VI shows that if only four popular spectral bands of MODIS are used in the cross-calibration process, the maximum averaged relative errors reach 7.09% for the cross-calibration method with the BOA BRDF model and 15.79% for the cross-calibration method with the TOA BRDF model, which indicates that the cross-calibration method with the TOA BRDF model is more sensitive to the SWIR spectral band information. Therefore, if other sensors with only four popular spectral bands (blue, green, red, and NIR) are treated as the reference to obtain the cross-calibration results of the WFV, then the cross-calibration method with the BOA BRDF model should be used to implement the cross-calibration of the WFV to improve the reliability of the cross-calibration results.

B. Influence of BRDF Correction on the Calibration Results

The TOA and BOA BRDF models are constructed to reduce the influence of the viewing geometric difference on the cross-calibration results. In this section, the effectiveness of the BRDF correction with the TOA and BOA BRDF models is discussed. The new cross-calibration coefficients are recalculated without the BRDF correction. The averaged relative errors between the OCCs and the new cross-calibration coefficients are listed in Table VII. Compared with Table V, Table VII shows that the averaged relative errors of the cross-calibration results are obviously increased with eight spectral bands. For the cross-calibration method with the BOA BRDF model, the maximum averaged relative error of the cross-calibration results increases from 6.48% to 10.70%. For the cross-calibration method with the TOA BRDF model, the maximum averaged relative error of the cross-calibration results increases from 10.77% to 14.79%. Therefore, the proposed TOA and BOA BRDF models are all effective in reducing the bidirectional reflectance effects of the DRCS, which can play an important role in our cross-calibration process.

C. Influence of SBAF Correction in the SWIR Spectral Band on the Calibration Results

Due to the lack of a corresponding reference spectral band, the SBAF correction coefficient in the SWIR spectral band is neglected in Section III-B. Therefore, the influence of this setting on the cross-calibration results with different BRDF models should be discussed. In this section, according to the previous related research method, the SBAF correction coefficient in the SWIR spectral band is reset to 1.1 and 0.9 to recalculate new cross-calibration coefficients, respectively [25]. Then, the averaged relative errors are calculated, and they are listed in Table VIII. The maximum averaged relative errors of the cross-calibration results after resetting the SBAF correction coefficient in the SWIR spectral band are close for each spectral band. The differences in the averaged relative errors are all less than 0.53%, which indicates whether the cross-calibration method with the BOA BRDF or TOA BRDF model is less impacted by the SBAF correction coefficient in the SWIR spectral band.

D. Influence of the Different Spectral Interpolation Methods on the Calibration Results

In our cross-calibration process, the continuous TOA and BOA spectral profiles of the investigated target are derived with the cubic polynomial interpolation method. In this section, another spectral interpolation method, the cubic spline

TABLE VIII

AVERAGED RELATIVE ERROR BETWEEN THE OCCS AND THE CROSS-CALIBRATION COEFFICIENTS WITH DIFFERENT BRDF MODELS AFTER RESETTING THE SBAF CORRECTION COEFFICIENT IN SWIR SPECTRAL BAND

The SBAF Correction Coefficient in SWIR Spectral Band	Spectral Band of WFV	The Averaged Relative Error	
		Cross-calibration Coefficients with the BOA BRDF Model (%)	Cross-calibration Coefficients with the TOA BRDF Model (%)
1.1	1	1.93	3.23
	2	5.61	3.30
	3	2.25	3.22
	4	5.30	1.31
	5	3.64	2.44
	6	5.41	10.50
	7	4.20	6.79
	8	6.46	3.04
0.9	1	1.95	3.27
	2	5.74	3.45
	3	2.15	3.00
	4	5.44	1.38
	5	3.75	2.67
	6	5.81	11.03
	7	4.18	6.51
	8	6.48	3.05

TABLE IX

AVERAGED RELATIVE ERROR BETWEEN THE OCCS AND THE CROSS-CALIBRATION COEFFICIENTS WITH DIFFERENT BRDF MODELS USING THE CUBIC SPLINE INTERPOLATION METHOD

Spectral Band of WFV	The Averaged Relative Error	
	Cross-calibration Coefficients with the BOA BRDF Model (%)	Cross-calibration Coefficients with the TOA BRDF Model (%)
1	2.02	3.55
2	6.10	4.80
3	1.82	1.58
4	5.16	1.47
5	3.59	4.44
6	5.44	12.55
7	4.10	5.54
8	6.38	3.00

interpolation method, is employed to fulfill the spectral interpolation to discuss the influence of the different spectral interpolation methods on the cross-calibration results.

Table IX shows that for the cross-calibration method with the BOA BRDF model, the maximum averaged relative error of the cross-calibration results is 6.38%, which is very close to that listed in Table V. However, for the cross-calibration method with the TOA BRDF model, the maximum averaged relative error of the cross-calibration results reaches 12.55%, which is higher than that listed in Table V, thus indicating that the cross-calibration method with the TOA BRDF model is more sensitive to the spectral interpolation method. Overall, these findings indicate that applying cubic polynomial interpolation with our cross-calibration methods using the BOA and TOA BRDF models can obtain more reliable cross-calibration results.

E. Uncertainty Analysis

Although many measures have been taken to reduce the influence of various factors on the cross-calibration results in our cross-calibration process, certain factors still cause uncertainty. In this section, the uncertainties caused by eight main factors (reference data, geometric mismatching, BRDF correction, spectral interpolation method, 6S model, AOT value, aerosol type, and SBAF correction) are analyzed, and the total uncertainty is calculated.

TABLE X

TOTAL CALIBRATION UNCERTAINTY OF CROSS-CALIBRATION RESULTS WITH THE BOA BRDF MODEL

Symbol	Spectral Band of WFV							
	1	2	3	4	5	6	7	8
MOD09 (%)	0.86	0.98	0.80	0.30	0.76	0.65	0.64	0.90
Geometric Mismatching (%)	1.77	2.11	2.42	2.31	2.73	2.56	1.36	2.40
BRDF Correction (%)	2.34	2.74	3.09	3.24	3.12	3.11	1.71	2.93
Interpolation Method (%)	0.31	0.98	1.01	0.59	1.05	1.44	2.26	0.19
6S Model (%)	1.60	1.60	1.60	1.60	1.60	1.60	1.60	1.60
AOT@550nm (%)	0.44	1.34	1.99	1.76	1.87	1.67	0.89	1.65
Aerosol Type (%)	1.33	1.92	2.19	3.24	2.43	2.93	0.95	2.20
SBAF correction (%)	0.15	0.20	0.20	0.30	0.39	0.43	0.27	0.18
Total Uncertainty(%)	3.74	4.69	5.33	5.70	5.57	5.73	3.82	5.03

1) Reference Data: Since the MOD09 product and MODIS image are treated as the reference data, the uncertainty caused by these reference data should be considered in our radiometric cross-calibration process. Therefore, according to a previous related study on the uncertainty of MODIS images and the MOD09 product, the new cross-calibration coefficients with the BOA and TOA BRDF models are calculated with the corresponding uncertainty of the reference data [19], [26]. Then, the maximum relative differences between the recalculated cross-calibration coefficients and the original cross-calibration coefficients are calculated, and they are listed in Tables X and XI. These values are taken as the uncertainty values associated with the reference data.

2) Geometric Mismatching: Due to the geo-positioning accuracy differences in the MODIS and WFV data, the geometric mismatching over the investigated target in the cross-calibration information extraction process will affect the cross-calibration results. Therefore, the uncertainty caused by geometric mismatching should be considered. In this section, the original DN extracted window of the WFV over the investigated target is shifted by 63 pixels [16]. The cross-calibration coefficients are recalculated with the new averaged DN value. Then, the maximum relative differences between the recalculated cross-calibration coefficients and the original cross-calibration coefficients are calculated and treated as the uncertainty values associated with the geometric mismatching.

3) BRDF Correction: In the process of our radiometric cross-calibration methods with the BOA and TOA BRDF models, time-series MOD09 and MODIS data are used to derive the BOA and TOA BRDF kernel-derived model coefficients over the DRCS, respectively. Therefore, the uncertainty caused by the related influencing factors needs to be taken

into account. Since only five spectral bands of MODIS are used to fulfill the BRDF correction, after the uncertainties of the corresponding factors in spectral bands 1–5 of MODIS are calculated, they are converted to the uncertainties of BRDF correction in eight spectral bands of the WFV. This uncertainty in spectral bands 1–5 of MODIS consists of four parts.

The first part of the uncertainty in spectral bands 1–5 of MODIS caused by the reference data can be obtained from a previous related study on the uncertainty of the MODIS image and MOD09 product [19], [26]. The TOA and BOA BRDF kernel-derived model coefficients listed in Table II are used to calculate the modeled TOA and BOA spectral reflectance, respectively. Then, the root-mean-square errors (RMSEs) between the modeled and observed TOA and BOA reflectance of time-series MOD02HKM and MOD09 are treated as the second part of the uncertainty in spectral bands 1–5 of MODIS caused by the kernel-derived model. The viewing geometry is increased by 0.1° to analyze the third part of the uncertainty in spectral bands 1–5 of MODIS caused by the observation angles using a calculation method similar to that of the second part. The TOA and BOA reflectance at a vertical observation angle are derived based on the observed TOA and BOA reflectance of the time-series MOD02HKM and MOD09 products with the kernel-derived model. The SDs of the TOA and BOA reflectance at a vertical observation angle are treated as the fourth part of the uncertainty in spectral bands 1–5 of MODIS caused by the stability of TOA and BOA spectral reflectance. Finally, the total uncertainties of the aforementioned factors in spectral bands 1–5 of MODIS are calculated by the square root method based on the four parts of the uncertainty, which are treated as the fluctuation of the TOA and BOA spectral reflectance in spectral bands 1–5 of MODIS to calculate the uncertainty for the BRDF correction in eight spectral bands of the WFV.

4) Spectral Interpolation Method: The maximum relative differences between the original cross-calibration coefficients with the cubic polynomial interpolation method and the new cross-calibration coefficients with the cubic spline interpolation method for each spectral band on different calibrated days are treated as the uncertainty for the spectral interpolation method.

5) 6S Model: In the process of applying the cross-calibration method with the BOA BRDF model, the equivalent BOA spectral reflectance is converted to the simulated TOA spectral reflectance with the 6S model. In the process of applying the cross-calibration method with the TOA BRDF model, the 6S model is also used to simulate the TOA spectral reflectance to calculate the SBAF correction coefficients. Therefore, the corresponding uncertainty caused by the 6S model should be taken into account [27].

6) AOT Value: Since the AOT at 550-nm values on different calibrated days is extracted from the MOD04_L2 product, the corresponding uncertainty of the AOT value is also considered in the total uncertainty of the cross-calibration [28].

7) Aerosol Type: The aerosol type of the DRCS is a mixture of desert and continental types. Therefore, the aerosol type is changed from desert aerosols to continental aerosols to analyze the uncertainty associated with the aerosol type.

TABLE XI

TOTAL CALIBRATION UNCERTAINTY OF CROSS-CALIBRATION RESULTS WITH THE TOA BRDF MODEL

Symbol	Spectral Band of WFV							
	1	2	3	4	5	6	7	8
Reference Sensor (%)	2.05	2.13	2.15	2.17	2.07	2.14	2.10	2.14
Geometric Mismatching (%)	1.80	2.08	2.66	2.41	2.84	2.43	1.44	2.34
BRDF Correction (%)	3.50	3.38	3.39	3.17	3.38	3.39	3.84	3.39
Interpolation Method (%)	0.45	2.13	2.62	0.62	3.08	2.73	3.92	0.18
SBAF correction (%)	1.67	1.63	1.64	1.66	1.66	1.68	1.83	1.63
Total Uncertainty (%)	4.76	5.25	5.72	4.87	6.00	5.68	6.32	4.93

8) SBAF Correction: For the cross-calibration method applied with the BOA BRDF model, the maximum differences between the new cross-calibration coefficients obtained by resetting the SBAF correction coefficient in the SWIR spectral band and the original cross-calibration coefficients for each spectral band are treated as the uncertainty values associated with the SBAF correction. For the cross-calibration method applied with the TOA BRDF model, the uncertainty of SBAF correction consists of four parts: resetting the SBAF correction coefficients in the SWIR spectral band, 6S model, AOT value, and aerosol type. Then, the total uncertainty caused by the SBAF correction is calculated by the square root method.

Tables X and XI show the uncertainties of the cross-calibration methods with the BOA and TOA BRDF models caused by various factors and the total uncertainty. The total uncertainties of the two cross-calibration methods are less than 5.73% and 6.32%.

VI. CONCLUSION

In this study, two radiometric cross-calibration methods applied with the TOA and BOA BRDF models are developed and compared to fulfill the radiometric cross-calibration of the GF-6/WFV sensor with eight spectral bands, and they can resolve the problem of a lack of reference spectral bands for four new spectral bands. The DRCS is taken as the investigated target, and MODIS images and products are treated as the reference information. The TOA and BOA spectral reflectance over the DRCS are extracted from the valid time-series MOD02HKM and MOD09 products to calculate the TOA and BOA BRDF kernel-derived model correction coefficients. Considering the BRDF correction and SBAF correction, the TOA and BOA spectral reflectance of MODIS are converted to the spectral reflectance under the geometric condition of the WFV. Then, the cubic polynomial interpolation method is used to obtain the interpolated continuous TOA and BOA spectral profiles. The simulated TOA and the equivalent BOA spectral reflectance of the WFV in eight spectral bands are derived with the RSRs of GF-6/WFV. For the cross-calibration method with the BOA BRDF model, the equivalent BOA spectral reflectance of the WFV is converted to the simulated TOA spectral reflectance with the aid of the 6S model. Finally, the

cross-calibration coefficients of the WFV are calculated with the DN value and the simulated TOA radiance.

The cross-calibration results on 19 days indicate that the cross-calibration coefficients have good stability, with SDs less than 0.40% with the BOA BRDF model and 0.50% with the TOA BRDF model. After using the OCCs to validate the cross-calibration results, the averaged relative errors of the cross-calibration coefficients are less than 6.48% with the BOA BRDF model and 10.77% with the TOA BRDF model, which proves that the cross-calibration method applied with the BOA BRDF model can obtain higher consistency with the OCCs than that applied with the TOA BRDF model.

The influences of the selected reference spectral band, spectral interpolation method, SBAF correction, and BRDF correction on the cross-calibration results are analyzed. Using five spectral bands of MODIS, the BOA BRDF model and the cubic polynomial interpolation method represent optimal cross-calibration schemes for GF-6/WFV sensor. Moreover, BRDF correction is an important step in the two cross-calibration method processes. However, the SBAF correction coefficient setting in the SWIR spectral band can be neglected with the two cross-calibration methods. Meanwhile, the total uncertainties of the two cross-calibration methods are less than 5.73% with the BOA BRDF model and 6.32% with the TOA BRDF model. In summary, the cross-calibration method applied with the BOA BRDF model is more suitable for GF-6/WFV sensor and can obtain higher consistency with the OCCs, good stability, and less uncertainty.

In the future, we will select more sites from radiometric calibration network (RadCalNet) established by the Working Group on Calibration and Validation of the Committee on Earth Observation Satellites (CEOS-WGCV) to further evaluate the proposed radiometric cross-calibration methods of GF-6/WFV sensor based on two BRDF models and then using the optimal cross-calibration method to fulfill the radiometric degradation detection of GF-6/WFV during its orbital lifetime.

ACKNOWLEDGMENT

The authors would like to acknowledge the China Centre for Resources Satellite Data and Application (CRESDA) for providing GaoFen-6 (GF-6) satellite imagery and the Moderate-Resolution Imaging Spectroradiometer (MODIS) Land Team for providing the MODIS data. They would also like to thank the anonymous reviewers.

REFERENCES

[1] Y. Qiao, X. B. Zheng, X. H. Wang, L. M. Zhang, W. N. Yi, and L. Y. Wang, "Whole-process radiometric calibration of optical remote sensors," *J. Remote Sens.*, vol. 10, no. 5, pp. 616–623, Sep. 2006.

[2] G. Chander, D. J. Meyer, and D. L. Helder, "Cross calibration of the Landsat-7 ETM+ and EO-1 ALI sensor," *IEEE Trans. Geosci. Remote Sens.*, vol. 42, no. 12, pp. 2821–2831, Dec. 2004, doi: 10.1109/TGRS.2004.836387.

[3] J. Lu, T. He, S. Liang, and Y. Zhang, "An automatic radiometric cross-calibration method for wide-angle medium-resolution multispectral satellite sensor using landsat data," *IEEE Trans. Geosci. Remote Sens.*, vol. 60, Apr. 2022, Art. no. 5604011, doi: 10.1109/TGRS.2021.3067672.

[4] P. M. Teillet, J. L. Barker, B. L. Markham, R. R. Irish, G. Fedosejevs, and J. C. Storey, "Radiometric cross-calibration of the Landsat-7 ETM+ and Landsat-5 TM sensors based on tandem data sets," *Remote Sens. Environ.*, vol. 78, nos. 1–2, pp. 39–54, Oct. 2001, doi: 10.1016/S0034-4257(01)00248-6.

[5] L. Liu, T. Shi, H. Gao, X. Zhang, Q. Han, and X. Hu, "Long-term cross calibration of HJ-1A CCD1 and Terra MODIS reflective solar bands," *Sci. Rep.*, vol. 11, pp. 1–14, Apr. 2021, doi: 10.1038/s41598-021-86619-y.

[6] J. Han, Z. Tao, Y. Xie, Q. Liu, and Y. Huang, "Radiometric cross-calibration of GF-4/PMS based on radiometric block adjustment," *IEEE Trans. Geosci. Remote Sens.*, vol. 59, no. 6, pp. 4522–4534, Jun. 2021, doi: 10.1109/TGRS.2020.3009740.

[7] Y. Zhao, L. Ma, C. Li, C. Gao, N. Wang, and L. Tang, "Radiometric cross-calibration of Landsat-8/OLI and GF-1/PMS sensors using an instrumented sand site," *IEEE J. Sel. Topics Appl. Earth Observ. Remote Sens.*, vol. 11, no. 10, pp. 3822–3892, Oct. 2018, doi: 10.1109/JSTARS.2018.2862638.

[8] A. Angal, X. Xiong, A. Wu, G. Chander, and T. Choi, "Multitemporal cross-calibration of the Terra MODIS and landsat 7 ETM+ reflective solar bands," *IEEE Trans. Geosci. Remote Sens.*, vol. 51, no. 4, pp. 1870–1882, Apr. 2013, doi: 10.1109/TGRS.2012.2235448.

[9] X. Zhou, D. Feng, Y. Xie, Z. Tao, T. Lv, and J. Wang, "Radiometric cross-calibration of GF-4/IRS based on MODIS measurements," *IEEE J. Sel. Topics Appl. Earth Observ. Remote Sens.*, vol. 14, pp. 6807–6814, 2021, doi: 10.1109/JSTARS.2021.3091977.

[10] Q. Zhou, L. Tian, J. Li, H. Wu, and Q. Zeng, "Radiometric cross-calibration of large-view-angle satellite sensors using global searching to reduce BRDF influence," *IEEE Trans. Geosci. Remote Sens.*, vol. 59, no. 6, pp. 5234–5245, Jun. 2021, doi: 10.1109/TGRS.2020.3019969.

[11] C. Niu *et al.*, "Radiometric cross-calibration of the ZY1−02D hyperspectral imager using the GF-5 AHSI imager," *IEEE Trans. Geosci. Remote Sens.*, vol. 60, Nov. 2022, Art. no. 5519612, doi: 10.1109/TGRS.2021.3131485.

[12] Q. Zhou, L. Tian, J. Li, and W. Li, "Assessment of bidirectional reflectance effects on desert and forest for radiometric cross-calibration of satellite sensors," *ISPRS J. Photogramm. Remote Sens.*, vol. 160, pp. 180–194, Feb. 2020, doi: 10.1016/j.isprsjprs.2019.12.007.

[13] W. Liu, J. Li, Q. Han, L. Zhu, H. Yang, and Q. Cheng, "Orbital lifetime (2008–2017) radiometric calibration and evaluation of the HJ-1B IRS thermal infrared band," *Remote Sens.*, vol. 12, no. 15, p. 2362, Jul. 2020, doi: 10.3390/rs12152362.

[14] M. M. Farhad, M. Kaewmanee, L. Leigh, and D. Helder, "Radiometric cross calibration and validation using 4 angle BRDF model between landsat 8 and sentinel 2A," *Remote Sens.*, vol. 12, no. 5, p. 806, Mar. 2020, doi: 10.3390/rs12050806.

[15] A. Yang *et al.*, "Radiometric cross-calibration of the wide field view camera onboard GaoFen-6 in multispectral bands," *Remote Sens.*, vol. 12, no. 6, p. 1037, Mar. 2020, doi: 10.3390/rs12061037.

[16] J. Han, Z. Tao, Y. Xie, H. Li, Q. Liu, and X. Guan, "A novel radiometric cross-calibration of GF-6/WFV with MODIS at the Dunhuang radiometric calibration site," *IEEE J. Sel. Topics Appl. Earth Observ. Remote Sens.*, vol. 14, pp. 1645–1653, Dec. 2021, doi: 10.1109/JSTARS.2020.3046738.

[17] J. Yu *et al.*, "Application study on double-constrained change detection for land use/land cover based on GF-6 WFV imageries," *Remote Sens.*, vol. 12, no. 18, p. 2943, Sep. 2020, doi: 10.3390/rs12182943.

[18] Y. Kang, Q. Meng, M. Liu, Y. Zou, and X. Wang, "Crop classification based on red edge features analysis of GF-6 WFV data," *Sensors*, vol. 21, no. 13, p. 4328, Jun. 2021, doi: 10.3390/s21134328.

[19] A. Angal, X. Xiong, and A. Shrestha, "Cross-calibration of MODIS reflective solar bands with sentinel 2A/2B MSI instruments," *IEEE Trans. Geosci. Remote Sens.*, vol. 58, no. 7, pp. 5000–5007, Jul. 2020, doi: 10.1109/TGRS.2020.2971462.

[20] B. Zhong, Y. Zhang, T. Du, A. Yang, W. Lv, and Q. Liu, "Cross-calibration of HJ-1/CCD over a desert site using Landsat ETM+ imagery and ASTER GDEM product," *IEEE Trans. Geosci. Remote Sens.*, vol. 52, no. 11, pp. 7247–7263, Nov. 2014, doi: 10.1109/TGRS.2014.2310233.

[21] X. Hu *et al.*, "Calibration for the solar reflective bands of medium resolution spectral imager onboard FY-3A," *IEEE Trans. Geosci. Remote Sens.*, vol. 50, no. 12, pp. 4915–4928, Dec. 2012, doi: 10.1109/TGRS.2012.2214226.

[22] S. Lacherade, B. Fougnie, P. Henry, and P. Gamet, "Cross calibration over desert sites: Description, methodology, and operational implementation," *IEEE Trans. Geosci. Remote Sens.*, vol. 51, no. 3, pp. 1098–1113, Mar. 2013, doi: 10.1109/TGRS.2012.2227061.

[23] X. Tian, Q. Liu, Z. Song, B. Dou, and X. Li, "Aerosol optical depth retrieval from Landsat 8 OLI images over urban areas supported by MODIS BRDF/Albedo data," *IEEE Trans. Geosci. Remote Sens. Lett.*, vol. 15, no. 7, pp. 976–980, Jul. 2018, doi: 10.1109/LGRS.2018.2827200.

[24] C. T. Pinto *et al.*, "Evaluation of the uncertainty in the spectral band adjustment factor (SBAF) for cross-calibration using Monte Carlo simulation," *Remote Sens.*, vol. 7, no. 9, pp. 837–846, Jun. 2016, doi: 10.1080/2150704X.2016.1190474.
[25] Y. Chen, K. Sun, D. Li, T. Bai, and C. Huang, "Radiometric cross-calibration of GF-4 PMS sensor based on assimilation of Landsat-8 oli images," *Remote Sens.*, vol. 9, no. 8, p. 811, Aug. 2017, doi: 10.3390/rs9080811.
[26] M. Broomhall, H. Chedzey, B. MeAtee, P. Fearns, and M. Lynch, "Validation of the extended suite of MOD09 and SMAC-processed reflectance products for Australian terrestrial supersites: A case study," in *Proc. AGU Fall Meeting*, 2014, Art. no. IN11B-3610.
[27] E. F. Vermote, D. Tanre, J. L. Deuze, M. Herman, and J. J. Morcette, "Second simulation of the satellite signal in the solar spectrum, 6S: An overview," *IEEE Trans. Geosci. Remote Sens.*, vol. 35, no. 3, pp. 675–686, May 1997, doi: 10.1109/36.581987.
[28] X. Chen *et al.*, "Joint retrieval of the aerosol fine mode fraction and optical depth using MODIS spectral reflectance over northern and eastern China: Artificial neural network method," *Remote Sens. Environ.*, vol. 249, Nov. 2020, Art. no. 112006, doi: 10.1016/j.rse.2020.112006.

Jie Han received the B.S. and M.S. degrees in science and technology of surveying and mapping from Henan Polytechnic University, Jiaozuo, China, in 2009 and 2012, respectively, and the Ph.D. degree in geography and geographic information system from the Institute of Remote Sensing and Digital Earth, Chinese Academy of Sciences, Beijing, China, in 2015.

He is currently an Associate Professor with the School of Urban and Environment Sciences, Xuchang University, Xuchang, China. He has worked on the radiomimetic and geometric processing of remote sensing images. His main research interest is the quantitative remote sensing applications in the visible/near-infrared.

Zui Tao was born in China in 1984. He received the B.S. degree from Henan University, Kaifeng, China, in 2005, the M.S. degree from Wuhan University, Wuhan, China, in 2008, and the Ph.D. degree from the Institute of Remote Sensing and Digital Earth (RADI), Chinese Academy of Sciences (CAS), Beijing, China, in 2012, all in cartography and geographic information system.

He is currently an Associate Professor with the Aerospace Information Research Institute, CAS. His research interests include the validation of remote sensing product, ecological, and environmental remote sensing.

Yong Xie received the B.S. and M.S. degrees in physics from Nanjing Normal University, Nanjing, China, in 2000 and 2004, respectively, and the Ph.D. degree in earth science and geoinformation system from George Mason University, Fairfax, VA, USA, in 2009.

He is currently a Professor with the School of Geographical Science, Nanjing University of Information Science and Technology, Nanjing. He has worked on the radiomimetic calibration and characterization of satellite remote sensor and science product validation with ground measurements.

Huina Li received the B.S. and M.S. degrees in electronic information engineering and communication and information system from Henan Polytechnic University, Jiaozuo, China, in 2009 and 2012, respectively.

She is currently an Assistant with the School of Electrical and Mechanical Engineering (Engineering Training Center), Xuchang University, Xuchang, China. Her main research interest is the remote sensing image processing in the visible/near-infrared.

Xiaoguo Guan received the M.S. degree in geodesy and surveying engineering from the China University of Mining and Technology (Beijing), Beijing, China, in 2013, and the Ph.D. degree in surveying and mapping engineering from the University of Information Engineering, Zhengzhou, China, in 2020.

She is currently a Lecturer with the School of Urban and Environment Sciences, Xuchang University, Xuchang, China. Her main research directions are the remote sensing image processing and BeiDou Navigation Satellite System/Global Navigation Satellite System (BDS/GNSS) precision positioning data processing.

Hang Yi received the B.S. and Ph.D. degrees in geophysics from the University of Science and Technology of China, Hefei, China, in 2011 and 2016, respectively.

He is currently a Lecturer with the School of Urban and Environment Sciences, Xuchang University, Xuchang, China. He has worked on the satellite gravity and global stress changes. His main research interest is the quantitative calculation of groundwater changes and drought conditions through satellite gravity observations.

Tingting Shi received the B.S. degree in geography and geographic information system from PLA Information Engineering University, Zhengzhou, China, in 2009, the M.S. degree in geography and geographic information system from the Institute of Remote Sensing and Digital Earth, Chinese Academy of Sciences, Beijing, China, in 2012, and the Ph.D. degree in geography and geographic information system from the Institute of Geographic Sciences and Natural Resources Research, Chinese Academy of Sciences, Beijing, in 2016.

She is currently an Associate Professor with the National Resource Center for Chinese Materia Medica, China Academy of Chinese Medical Sciences, Beijing. She has worked on the remote sensing classification of land use/land cover. Her main research interest is remote sensing monitoring of medicinal plants.

Gengke Wang received the B.S. and M.S. degrees in computer science and technology and applied mathematics from Henan University, Kaifeng, China, in 2006 and 2011, respectively. He is currently pursuing the Ph.D. degree in signal and information processing with the Aerospace Information Research Institute, Chinese Academy of Sciences, Beijing, China.

He is currently also an Assistant Research Fellow with the Aerospace Information Research Institute. He has worked on the imaging simulation of optical remote sensing satellite. His main research interest is the principle of remote sensing imaging in the visible/near-infrared.